Geometry-based MPC tracking and modeling algorithm for time-varying UAV channels

Rodríguez-Piñeiro, José ; Huang, Zeyu ; Cai, Xuesong; Domınguez-Bolano, Tomas; Yin, Xuefeng

Published in:
IEEE Transactions on Wireless Communications

DOI (link to publication from Publisher):
10.1109/TWC.2020.3044077

Publication date:
2021

Document Version
Accepted author manuscript, peer reviewed version

Geometry-based MPC Tracking and Modeling Algorithm for Time-Varying UAV Channels

José Rodríguez-Piñeiro, Zeyu Huang, Xuesong Cai, Tomás Domínguez-Bolaño, and Xuefeng Yin, *Member, IEEE*

Abstract

In parallel with the decrease in cost, size and weight of Unmanned Aerial Vehicles (UAVs) and the increase of their flight autonomy, many commercial applications are rapidly arising. Most of those applications rely on a communications system between a terrestrial base station and the UAV. Due to the UAV movement, time-variant channel models are required. In this paper, we propose a geometrical model for the channel Multipath Components (MPCs) evolution with the UAV flight that supports MPCs that are born and die in several occasions due to blockages. Based on this model, the novel Geometry-Based Spatial-Consistent MPC Tracking Method (GSTM) is proposed and its performance on channel MPCs tracking was shown both by simulations and by an Air-to-Ground (A2G) low-height UAV measurement campaign. The GSTM also provides the parameters of a geometrical model of the evolution of the main MPCs of the channel, which allows to identify the scatterers that lead to the MPCs and greatly contributes to the understanding of the propagation mechanisms in A2G environments. The

J. Rodríguez-Piñeiro and X. Yin are with the College of Electronics and Information Engineering, Tongji University, Shanghai, China. (e-mail: j.rpineiro@tongji.edu.cn and yinxuefeng@tongji.edu.cn).

Z. Huang is with the CD-Lab for Dependable Wireless Connectivity, Institute of Telecommunications, TU Wien, Vienna, Austria. (e-mail: zeyu.huang@tuwien.ac.at).

X. Cai is with the Wireless Communication Networks Section, Department of Electronic Systems, Aalborg University, Aalborg, Denmark. (e-mail: xuc@es.aau.dk).

T. Domínguez-Bolaño is with the Department of Computer Engineering, University of A Coruña, A Coruña, Spain. (e-mail: tomas.bolano@udc.es).

Corresponding author: Xuefeng Yin (e-mail: yinxuefeng@tongji.edu.cn).

This work was supported by the National Natural Science Foundation of China (NSFC) under Grants 61850410529 and 61971313; as well as by the Xunta de Galicia (ED431G2019/01), the Agencia Estatal de Investigación of Spain (TEC2016-75067-C4-1-R, RED2018-102668-T, PID2019-104958RB-C42) and ERDF funds of the EU (AEI/FEDER, UE). The financial support by the Austrian Federal Ministry for Digital and Economic Affairs and the National Foundation for Research, Technology and Development is gratefully acknowledged.

correctness of the MPC tracking is proven to be higher than 90% and the results show that the model obtained by the GSTM includes more than 95% of the received power.

Index Terms

UAV; Air-to-Ground; Communications channels; Time-varying channels; MPCs tracking

I. Introduction

Unmanned Aerial Vehicles (UAVs) have shown to be able to contribute to support a broad number of applications in modern societies, even in the form of UAV swarms. Some examples of applications gaining importance are precise land mapping by aerial imagery [1], coordinated application of chemical substances in agriculture [2], remote sensing, forests inventory and tree species classification [3], operations in inaccessible areas, or delivery of goods or search and rescue missions [4]. Provisioning of temporary network access after disasters or in saturated environments by means of UAVs is also one of the scenarios addressed by the fifth generation (5G) communication systems [5] due to the ability of the UAVs for fast deployments. For most of the applications mentioned above, a connection between the UAV and an operator (manual or automated) is required, which should rely on a wireless connection. A natural choice would be the use of ground Long Term Evolution (LTE) or 5G deployments. UAV communications in LTE have attracted and are still attracting a considerable amount of interest in 3rd Generation Partnership Project (3GPP) standards from the Releases 15-17 [6].

The communications signal at the receiver is commonly expressed as a superposition of Multipath Components (MPCs), consisting each of them of certain portion of the transmitted energy that reaches the receiver following a specific physical path. Each MPC can be characterized by a set of parameters, such as the transmission delay, the Doppler frequency or the relative amplitude. In time-variant scenarios, the number of MPCs, as well as the parameters associated to each MPC will usually vary with the time, resulting in time-evolving MPCs, thus also time-evolving clusters of MPCs [7]. Due to long periods under blockage, MPCs can disappear at a specific time instant and reappear much later, as we have shown for the specific case of Air-to-Ground (A2G) communications for UAVs in our previous work [8]. Although the non-stationary nature of channels has been considered in Geometry-Based Stochastic Channel Models (GSCMs) (e.g., see [9]), the complete dynamic behaviors of MPCs need to be addressed, including their birth/death processes [10]. Tracking of time-varying MPCs that can relate distant MPCs (e.g.,

due to blockage) as a single time-evolving MPC can avoid the loss of spatial-consistency of the channel models.

Algorithms of different types have been proposed to track time-variant MPCs. In [11], recursive expectation-maximization (EM) and space-alternating generalized expectation-maximization (SAGE)-inspired algorithms have been proposed, which provide a quick update on estimates given augmented data. In [12], an extended Kalman filter was derived to track the delays, angles and amplitudes of MPCs. The algorithm proposed can track the evolution of "continuous" MPCs, being unable to deal with blockage scenarios (i.e., if a MPC disappears and later reappears, the second appearance will be considered as a newly-born MPC). Similarly, a Kalman Enhanced Super Resolution Tracking (KEST) algorithm has been proposed in [13]. It is noteworthy that the KEST exploits the output of a maximum likelihood (ML) estimator rather than the received signals as the measurement model. The time-variant model order (number of MPCs) is also determined, although the proposal cannot deal with blockage situations (as in the previous work, non-continuous trajectories of MPCs cannot be associated to a single time-evolving MPC). A particle filter was also proposed in [14] to overcome the possible inaccurate-linearization problem as noted in [13] with the drawback of higher complexity. In [15], MPC trajectories are obtained by maximizing the total moving probability between neighboring snapshots, hence non-continuous MPCs cannot be tracked. Connection-based or minimum-distance based algorithms can be found in [16]–[18] where the pairs of MPCs with smallest distance are linked. These approaches can deal with blockage situations, by connecting tracked MPCs as a single time-evolving MPC based purely on a metric distance criterion. This means that two tracked MPCs can be linked as a single time-evolving MPC if the differences between the values of the parameters of the two tracked MPCs are low enough. In [19], an image-processing technique was proposed to track MPC trajectories directly using time-variant power delay profiles (PDPs). [20] presents a clustering and tracking method that includes an iterative process joining long-lifetime clusters that were broken into smaller lifetime ones. For this, a linear fitting is considered and only two clusters are joined in each iteration. [21] presents MPC tracking results for a vehicular communication scenario, exhibiting MPC birth and death processes. A method for long-term tracking of the MPCs evolution is proposed, which uses the evolution of the MPCs in a time-window to estimate the delay of the adjacent time-windows and look for candidate MPCs to be linked together. [22] considers the temporal evolution of the MPCs as a basis for MPC clustering. The proposal identifies the trajectories of individual MPCs first and then clusters the MPCs based

on the identified trajectories. Close MPCs between consecutive snapshots can be considered as a single MPC based on a distance metric. In [23], a MPC tracking algorithm in the delay-angle space is proposed. Linear polynomials defined piecewise in the multidimensional MPC space are used for the MPC tracking.

Most of the previously mentioned MPC tracking approaches fail in dealing with blockage situations. In many cases blockages are just not considered and when a MPC is born it will be considered as a new MPC (e.g., [11]–[15]). In others, such as [16]–[18], [21], [22], the only criteria to consider separated MPCs as a single time-evolving MPC is the difference between the values of the parameters of the MPCs. However, if the time interval between the MPCs is large, their respective parameters can be quite different. In others, such as [20], [23] only linear fits are be used to decide whether to join separated MPCs as a single time-evolving MPC. However, we will see that a linear fitting is not always a good approximation, especially when the time distance between the MPCs is large. Furthermore, for many of the approaches, connecting MPC trajectories as a single time-evolving MPC is done in an iterative fashion by considering only two trajectories at a time, such as in [16]–[18], [20]. In this work, the so-called Geometry-Based Spatial-Consistent MPC Tracking Method (GSTM) is proposed. The GSTM is able to track MPCs that disappear for long periods of time due to blockages.. Based on some realistic assumptions about the typical propagation environments for A2G UAV communications in urban or suburban scenarios a quadratic fitting is proposed to track the evolution of the delay of MPC trajectories over time. Different from the previous methods, this enables to predict the value of delay of the MPCs even though they disappear for long periods of time and solves the inaccuracies caused by assuming linear fittings. Furthermore, different from other methods, all the estimated MPCs are considered at a time when fitting MPC trajectories instead of just iteratively processing pairs of MPCs. This leads to more accurate fits of the MPC trajectories. What is more, we will show that the evolution of many MPCs can be geometrically modeled up to some point, including their successive birth/death events due to eventual blockages from elements of the environment. Under some circumstances, these geometrical models can be used for identifying the elements of the propagation environment originating the MPCs. The performance of the method is firstly evaluated by Monte-Carlo simulations using propagation scenarios randomly generated, showing that the GSTM is capable of tracking the MPCs that include birth/death events and extract the corresponding geometrical models for their variation. Secondly, the practical applicability of the algorithm is shown by analyzing the received signals

for an actual measurement campaign for A2G low-height UAV in suburban environments. The main contributions of this paper are summarized in the following points:

- As a contribution to the time-variant channel modeling for A2G UAV communications, a method for tracking the channel MPCs, namely the GSTM, was proposed. By taking advantage of realistic assumptions about typical propagation environments for this kind of communications, the GSTM exhibits the following advantages:
  1) It can effectively detect the birth/death processes for the different MPCs, even though eventually the MPCs disappear for long periods of time (e.g., they are temporarily obstructed by large buildings close to the flight route). In other words, it can detect the long-term spatial consistency of the MPCs;
  2) The GSTM is not only capable of tracking the variation of the MPCs, but also provides the parametrization of a geometrical model for the main MPCs. This model can be used the for the channel prediction, channel inference or, in particular, to help to identify the objects originating the different MPCs. The numerical results show that in a practical situation the obtained geometrical model for the main MPCs includes more than 95% of the received power.
  3) Although our study is mainly focused on A2G UAV communications, the GSTM could be applied to other scenarios involving relative movement between the transmitter and receiver with frequent line-of-sight (LoS) conditions between the transmitter and the main scatterers, as well as between those scatterers and the receiver. This can be, for example, the case of Vehicle-to-Infrastructure (V2I) communications in urban or suburban environments.
- The performance of the GSTM is shown by Monte-Carlo simulations using propagation scenarios randomly generated and by analyzing the received signals from a measurement campaign for A2G low-height UAV flights in a suburban environment. The simulation results show that, even in the presence of estimation noise, the the tracking of the evolution of the MPCs, including their birth/death events, is correct for more than 90% of them.
- The obtained results can explain the propagation mechanisms that lead to non-intuitive effects in the communications channel characteristics described in our previous publications, such as [8], [24], stating the basis for new non-stationary channel models.

The structure of the rest of this paper is as follows: Section II presents the basics of the geo-

metrical approach proposed to model the evolution of the channel MPCs. Section III introduces the GSTM. Section IV firstly introduces the details of the performed measurement campaign and secondly presents the results of applying the GSTM to the acquired signals during the measurements. Finally, Section V contains the main conclusions of the performed study.

II. Basics of the Geometrical Model for the MPCs

In practice, in order to estimate the channel parameters for a specific time instant, a certain set of signal samples is collected and further processed in some way. This set of samples is usually denoted as "snapshot". For the i-th snapshot we can define the noise-free time-varying channel impulse response by means of

$$h_i(t,\tau) = \sum_{l=1}^{L} \alpha_{i,l} \exp\{j2\pi\nu_{i,l}t\}\delta(\tau - \tau_{i,l}), \tag{1}$$

where t is the time variable, τ is the delay variable, L is the number of waves or paths, $\alpha_{i,l} \in \mathbb{C}$ is the l-th path amplitude, $\nu_{i,l} \in \mathbb{R}$ and $\tau_{i,l} \in \mathbb{R}$ are the respective Doppler frequency and delay for the l-th path, and $\delta(\cdot)$ is the Dirac delta function.

For some sort of environments, the channel MPC estimates for near snapshots will probably exhibit a clear relationship among them. For example, if the reflection of the signal in a building leads to a MPC estimate for a specific snapshot, it is expectable that another MPC estimate with similar values of power, Doppler frequency and delay will be detected in the next snapshot as well. If the total distance traveled by the signal increases with time (due to the relative speed between the transmitter and the receiver), the power of the MPC estimates for consecutive snapshots will decrease in general, whereas the delay will increase. The evolution of the Doppler frequency over different snapshots can also follow different patterns depending on aspects such as the relative speed between the transmitter and the receiver.

As an example, consider the simplified case imaged in Fig. 1a[1]. A Base Station (BS), denoted by B, is placed at the origin and with height h_{B}, communicates with an UAV, namely U, which flies at a constant height h_{U} along the X axis with a speed v. We denote the instantaneous position of the UAV, determined by its horizontal distance[2] to the BS (i.e., the distance over the X axis),

[1]Note that this example is provided for illustrative purposes and does not correspond to an actual propagation environment. Hence, several simplifications have been considered.

[2]In the following, we will denote by "horizontal distances" the distances measured on the XY plane, i.e., without taking into account the height of the elements.

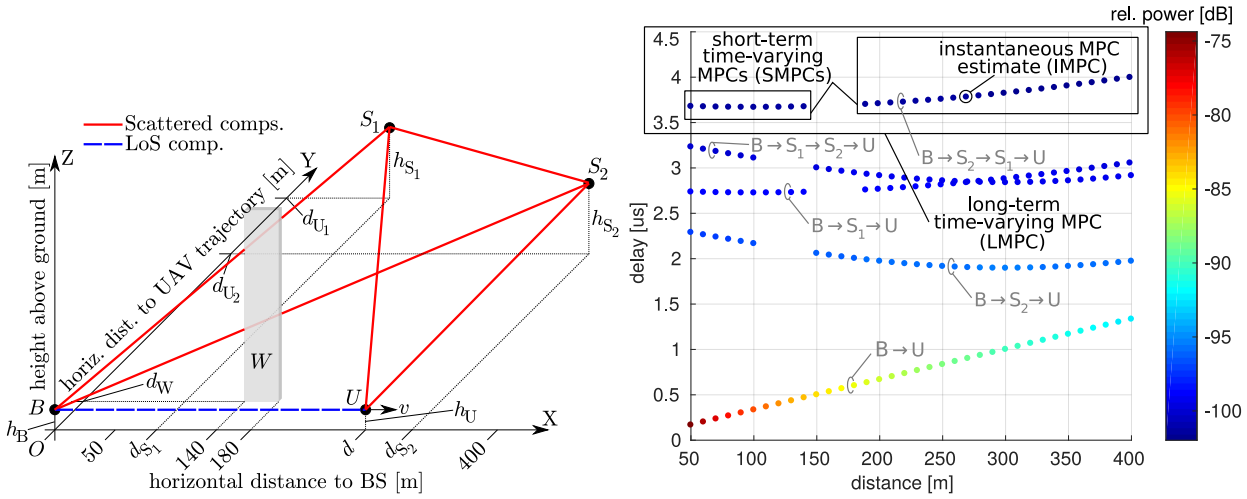

(a) Flight scenario.

(b) Obtained PDP.

Fig. 1: A2G simplified scenario: an UAV flies while communicating with a static terrestrial BS. The propagation environment includes a single scatterer as well as a non-reflecting wall.

as d. There are two punctual scatterers, respectively denoted by S_1 and S_2, placed at horizontal distances from the BS given by d_{S_1} and d_{S_2}, respectively and at horizontal distances from the flight trajectory (measured over the Y axis) given by d_{U_1} and d_{U_2}, respectively. The heights of the scatterers are respectively denoted by h_{S_1} and h_{S_2}. Additionally, there is a non-reflecting (i.e., that does not produce new scattering components) wall, denoted by W, at a horizontal distance d_{W} from the flight trajectory. We consider that the height of the wall is much larger than the heights of the other elements of the scenario and its thickness is negligible[3]. Without loss of generality, let consider as an example the values $d_{\mathrm{S}_1} = 300\,\mathrm{m}$, $d_{\mathrm{S}_2} = 100\,\mathrm{m}$, $d_{\mathrm{U}_1} = 200\,\mathrm{m}$, $d_{\mathrm{U}_2} = 400\,\mathrm{m}$, $h_{\mathrm{S}_1} = h_{\mathrm{S}_2} = 60\,\mathrm{m}$, $d_{\mathrm{W}} = 40\,\mathrm{m}$, $h_{\mathrm{B}} = 15\,\mathrm{m}$, $h_{\mathrm{U}} = 15\,\mathrm{m}$ and $v = 5\,\mathrm{m/s}$. In this simplified scenario, we will consider the propagation of the specular components from the BS to the UAV (marked in Fig. 1a as a dashed blue line) and the scattered components originated at the BS and reflected in the scatterers. In particular, we consider the scattered components $B \to S_1 \to U$, $B \to S_2 \to U$, $B \to S_1 \to S_2 \to U$ and $B \to S_2 \to S_1 \to U$. The scattered components are represented in Fig. 1a by solid red lines.

[3]In this simplified model, the wall will not allow the penetration of the signals and no reflection or diffraction effects are produced.

The propagation distance for any specular component can be described as

$$d_p\left(d\right) = d_{p^{\text{FH}}} + d_{p^{\text{LH}}}\left(d\right), \tag{2}$$

where d is the position of the UAV (see Fig. 1a). The term depeding on d in (2) will be given by the "last hop" of the signal, i.e., the transmission of the signal from the last scatterer (or from the BS, for the case of the LoS component), whereas the constant term will be given by the distance traveled by the signal before the "last hop" (if any). Hence, if we take the case of the specular component $B \rightarrow S_1 \rightarrow S_2 \rightarrow U$ as an example, we would have $d_{p^{\text{FH}}} = \|B - S_1\|_2 + \|S_1 - S_2\|_2$, where $\|\cdot\|_2$ denotes the Euclidean distance. The term corresponding to the last hop can be written as

$$d_{p^{\text{LH}}} = \|S - U\|_2 = \sqrt{(d_{\text{S}} - d)^2 + d_{\text{U}}^2 + (h_{\text{S}} - h_{\text{U}})^2}, \tag{3}$$

where $\|\cdot\|_2$ denotes the Euclidean distance, S is the last scatterer (the BS in the case of the LoS component), d_{S} the horizontal distance between the scatterer and the BS, d_{U} the distance between the scatterer and the flight trajectory and h_{S} the height of the scatterer. $\left(d_{p^{\text{LH}}}\right)^2$, as given in (3), can be written as a hyperbolic curve with respect to the horizontal distance between the transmitter and the receiver, d, as

$$Ad^2 - C\left(d_{p^{\text{LH}}}\right)^2 + Dd + Ed_{p^{\text{LH}}} + F = 0, \tag{4}$$

with $A = 1$, $C = 1$, $D = -2d_{\text{S}}$, $E = 0$ and $F = d_{\text{S}}^2 + d_{\text{U}}^2 + (h_{\text{S}} - h_{\text{U}})^2$. This way, $d_p\left(d\right)$ can be obtained in general as the square root of an hyperbolic curve plus a constant term.

A graphical representation of the expected MPCs approaching the receiver can be obtained by means of the PDP, which exhibits how much power arrives at the receiver with a certain delay τ. In practice, the PDP is obtained as the power for a certain timespan over which the channel is quasi-stationary [25]. Following the same approach as in our previous works [8], [26], we can calculate the PDP for the i-th snapshot (see (1)), namely the "instantaneous" PDP, as [27]:

$$P_i(\tau) = \sum_{l=1}^{L} |\alpha_{i,l}|^2 \delta(\tau - \tau_{i,l}). \tag{5}$$

It is straightforward to obtain the PDP for the simplified scenario provided if we consider space-free conditions for the power attenuation and no power loss in the reflections, hence just applying the well-known Friis transmission equation [28] for each signal component[4] and using

[4]For convenience we have just assumed that both components (the direct one and the scattered one) have equivalent initial power and that the operating frequency is $2.5\,\text{GHz}$.

(2). The obtained PDP is shown in Fig. 1b, where the snapshots are acquired with a period of 5 s. Each dot in Fig. 1b represents the estimate of a MPC for a specific snapshot. The relative received power is represented by the dot color, whereas the X axis represents the horizontal distance between the BS and the UAV (for the time instant corresponding to the MPC estimate) and the Y axis the delay of the MPC estimates. The straight line corresponds to the LoS component and the curved ones to the scattered ones. Parallel curves correspond to components with a common "last hop" (see (2)). Additionally, Fig. 1b gives some insights on the basic properties of the proposed geometrical model. This way, for the curves defined by the MPCs of the scattered components, we can observe that *(1)* the vertex of the curve (i.e., the point for which the delay is minimum) is related with the horizontal distance between the "last hop" scatterer and the BS; *(2)* the eccentricity of the curve (i.e., the measure of how small the maximum slope is) is related with the horizontal distance between the "last hop" scatterer and the UAV flight trajectory; and *(3)* the absolute delay values will increase –hence the curve will be shifted along the Y axis– with the scattering order[5]. In order to study the time-variant behavior of the MPCs, we define the following concepts, which are illustrated in Fig. 1b:

- **Instantaneous MPC estimate (IMPC)**: estimated channel MPC for a specific snapshot, represented as dots in Fig. 1b.
- **Short-term Time-Variant MPC (SMPC)**: "continuous" set of IMPCs that correspond to a single actual MPC that evolves in time. "Continuous" in this context means that if we consider the IMPCs ordered by their snapshot index, the difference between the snapshot indexes of two consecutive IMPCs is below a certain threshold. The SMPCs show the evolution of a MPC during a period in which no birth/death processes occur. By considering a threshold of a single snapshot, two sample SMPCs are labeled in Fig. 1b, both corresponding to the scattered component.
- **Long-term Time-Variant MPC (LMPC)**: defined to account for the case in which an MPC dies and is reborn. A LMPC is formed by a set of SMPCs that correspond to a single actual MPC that dies and is re-born (probably more than once). Additionally, it is said that an LMPC is active for a specific snapshot (or time instant) if it contains an IMPC for

[5]In the general case it is not possible to unambiguously obtain the position of a scatterer from the geometrical model, especially for scattering orders higher than 1. However, with the help of the geometrical model, we can find a plane in which the scatterer should be (the degrees of freedom defining the exact position of the scatterer are the height of the scatterer and the constant term in (2) when the scattering order is higher than 1).

that snapshot, and inactive otherwise. An example of LMPC, comprised by two SMPCs, is shown in Fig. 1b. It is clear that the MPC caused by the scattering component dies when the wall obstructs the propagation between the scatterer and the UAV and it is re-born when the obstruction disappears. It can be seen that the LMPC is inactive during the period of obstruction by the wall and active for any other snapshot. The LMPCs show the potentially non-continuous evolution of a MPC during a period in which birth/death processes can occur.

In practice, reflections are not caused by a single point of the nearby objects. Indeed, as firstly proposed by Saleh-Valenzuela in 1987 [7], in most of the cases clusters of MPCs can be observed instead of individual MPCs. However, in many cases, the resolution of the measurements or the estimation techniques used is not high enough to distinguish the actual MPCs of the clusters, and a single MPC is detected instead for each cluster, which is assumed to correspond to the centroid or nominal of the cluster [29], [30]. This way, tracking the individual MPCs is still interesting, rather than considering only the tracking of MPC clusters. Indeed, in Section IV-B we will show that the evolution of the main MPCs can still be accurately described by means of curves in the PDP in practical cases. Additionally, many other not so regular elements can cause multiple random scattering components not exhibiting a clear trend over snapshots (e.g., reflections in the structure of the UAV itself, that could exhibit fast changing behaviors with the inevitable variations of the orientation of the UAV due to the wind). In this work we will mainly focus on the study of the MPCs that exhibit a regular trend over time with the flight of the UAV. The empirical results in Section IV-B will show that in a realistic case more than $95\,\%$ of the received power will be concentrated in such MPCs.

III. Geometry-Based Spatial-Consistent MPC Tracking Method (GSTM)

In this paper a method for detecting and characterizing the time-variant behavior of the channel MPCs, namely the GSTM, is proposed. The GSTM comprises two steps, described as follows:

1) **Detection of SMPCs**: A metric distance based on the differences of delay, Doppler, power and BS-UAV horizontal distance is proposed to group IMPCs meeting certain metric distance criteria into SMPCs. In particular, this step will exploit the short-term spatial consistency of the delay, Doppler frequency and power of the IMPCs.
2) **Detection of LMPCs**: The geometrical properties of the SMPCs are exploited to identify which ones are more likely to define a LMPC. In particular, this step will take advantage

of the long-term spatial consistency of the delay of the IMPCs. This will be also the basis for the establishment of an analytical geometrical model for the LMPCs.

The two aforementioned steps are described in detail in Sections III-A and III-B, respectively. Finally, Section III-C will present some insights in the analysis of the performance of the proposed method.

A. Detection of Short-term Time-Variant MPCs

The method for detecting SMPCs is detailed in Algorithm 1. The algorithm will group IMPCs expected to represent a unique MPC evolving over time (or, equivalently, over different snapshots). At the output of the algorithm, each IMPC must belong to one (and only one) SMPC. In order to select eligible IMPCs to belong to a common SMPC, a multi-dimensional metric distance between different IMPCs is defined. Two IMPCs are qualified to belong to a common SMPC if the metric distance between them does not exceed a predefined multi-dimensional threshold.

For convenience, let denote each IMPC as a four-dimensional vector $\mathbf{u} = (u_1, u_2, u_3, u_4)^{\mathrm{T}}$, where u_1 denotes the horizontal distance between the UAV and the BS for the snapshot corresponding to the IMPC, and u_2, u_3, and u_4 denote the IMPC power, delay and Doppler frequency, respectively; whereas $(\cdot)^{\mathrm{T}}$ is the transpose operator. Then, the metric distance between the IMPCs $\mathbf{u}^1 = (u_1^1, u_2^1, u_3^1, u_4^1)^{\mathrm{T}}$ and $\mathbf{u}^2 = (u_1^2, u_2^2, u_3^2, u_4^2)^{\mathrm{T}}$, namely $\mathbf{DP}^{\mathbf{r}}(\mathbf{u}^1, \mathbf{u}^2)$, is the four-dimensional vector

$$\mathbf{DP}^{\mathbf{r}}(\mathbf{u}^1, \mathbf{u}^2) = \begin{cases} \left(\frac{\left|u_1^1 - u_1^2\right|}{r_1}, \ldots, \frac{\left|u_4^1 - u_4^2\right|}{r_4} \right)^{\mathrm{T}}, \text{ if } u_1^1 \neq u_2^1 \\ \left(\infty, \frac{\left|u_2^1 - u_2^2\right|}{r_2}, \ldots, \frac{\left|u_4^1 - u_4^2\right|}{r_4} \right)^{\mathrm{T}}, \text{ if } u_1^1 = u_1^2, \end{cases} \tag{6}$$

where $\mathbf{r} = (r_1, r_2, r_3, r_4)^{\mathrm{T}}$ is a vector with some predefined values. More specifically, r_1, r_2, r_3 and r_4 are thresholds corresponding to the maximum allowed differences in terms of horizontal distance[6], power, delay and Doppler frequency, respectively, so that two IMPCs can be assumed to belong to a common SMPC. In other words, the IMPCs $\mathbf{u}^1$ and $\mathbf{u}^2$ are qualified to belong to a common SMPC if none of the four components of $\mathbf{DP}^{\mathbf{r}}(\mathbf{u}^1, \mathbf{u}^2)$ exceeds 1. By adjusting

[6]In the actual implementation, the distance threshold is specified as a number of consecutive snapshots. This way, if for some time instant the estimates are not available (i.e., one snapshot is not available due to some problem with the reception of the signal, for example), the actual distance threshold will not take the missing snapshot into account.

the values of the different components of $\mathbf{r}$ it is possible to increase or decrease the sensitivity of the comparison of different IMPCs. For example, if the flight speed of the UAV is increased, probably r_2 should be increased since more power difference between IMPCs of consecutive snapshots can be expected; the same would probably hold to r_3. Currently there is not an automatic way for adjusting the threshold values and in our tests we have done it manually (see Table IV in Section IV-B). Note that, according to (6), two IMPCs corresponding to a common snapshot cannot be included in the same SMPC. This is due to the algorithm selects IMPCs from different snapshots, so that they can actually represent the evolution of a single MPC over time (or, equivalently, over different snapshots). Finally, it is worth noting that a weighting vector $\mathbf{w} = (w_1, w_2, w_3, w_4)^{\mathrm{T}}$ is used in the Algorithm 1 in order to give more weight to some of the components of the distance metric. This way, if for example the Doppler frequency estimates were very noisy, the value of w_4 can be reduced to minimize their impact in the results. Setting $w_4 = 0$ would simply not consider the Doppler frequency for the evaluations. The relative difference between the values of the different components of $\mathbf{w}$ will determine which components have more importance when comparing two IMPCs.

The Algorithm 1 groups the IMPCs into SMPCs based on the exposed metric distance. The method starts with all the IMPCs ordered by decreasing power[7]. The algorithm starts with a SMPC in which only the maximum power IMPC is included and, in each iteration, finds all the IMPCs that can be integrated in the SMPC based on the presented metric distance. Only a single IMPC, the one at minimum distance to any of the IMPCs already in the SMPC, is added to the SMPC. Once this is done, the search of all the IMPCs that can be integrated in the SMPC starts again. If no IMPC meets the metric distance criterion, a new SMPC is created, comprising only by the IMPC whose power is the highest among those that do not belong to any SMPC yet. The process continues until all the IMPCs are integrated in a SMPC.

Fig. 2a shows the results of applying the Algorithm 1 to the case shown in Fig. 1b. The IMPCs belonging to a common SMPC are joined with a line, hence being each line comprised by the set of all segments joining pairs of consecutive IMPCs in the SMPC. The color of the line is defined by the average power of all the IMPCs in the SMPC.

[7]The algorithm starts creating SMPCs from the IMPCs whose power is the highest since in general those can be regarded as the most reliable (less noisy) estimates.

Algorithm 1 Detection of SMPCs

Let denote by $\mathbf{u} = (u_1, u_2, u_3, u_4)^{\mathrm{T}}$ each IMPC, where u_1 denotes the horizontal distance between the UAV and the BS, and u_2, u_3 and u_4 denote the IMPC power, delay and Doppler frequency, respectively. Finally, $(\cdot)^{\mathrm{T}}$ is the transpose operator.

Let $\mathcal{U} = \{\mathbf{u}^1, \mathbf{u}^2, \ldots, \mathbf{u}^{|\mathcal{U}|}\}$ be defined as the set of ungrouped IMPCs (IMPCs not belonging to any SMPC, initially all of them) where $u_2^1 \geq u_2^2 \geq \cdots \geq u_2^{|\mathcal{U}|}$ (i.e., IMPCs are ordered by descending power value) and the operator $|\cdot|$ denotes the number of elements of a set.

Initialize $N := 0$ *(index of the current SMPC)*

while $\mathcal{U} \neq \{\emptyset\}$ *(still ungrouped IMPCs)* **do**

Create a new SMPC including the first ungrouped IMPC (the one with the largest power):

$N \leftarrow N + 1$

$\mathcal{U} \leftarrow \mathcal{U} - \{\mathbf{u}^m\}, m = \arg\min_{i=1,2,\ldots,|\mathcal{U}|} \mathbf{u}^i \in \mathcal{U}$

$\mathcal{G}^N := \{\mathbf{u}^m\}$

Look for IMPCs that can be integrated in the current SMPC:

Candidate IMPCs not evaluated yet $\leftarrow$ YES

while Candidate IMPCs not evaluated yet $=$ YES **do**

Create an empty set and fill it with the ungrouped IMPCs that meet the metric distance criterion to be included in the current SMPC:

$\mathcal{V} := \{\emptyset\}$

for $i = 1, 2, \ldots, |\mathcal{U}|$ **do**

if $\mathbf{DP^t}(\mathbf{g}, \mathbf{u}^i) \leqq (1,1,1,1)^{\mathrm{T}}, \forall \mathbf{g} \in \mathcal{G}^N$ $^{(*)}$ **then**

$\mathcal{V} \leftarrow \mathcal{V} \cup \mathbf{u}^i$

end if

end for

if $\mathcal{V} \neq \{\emptyset\}$ **then**

If there are candidate IMPCs to be included in the SMPC, select the best one based on the metric distance and update the SMPC:

$\mathcal{G}^N \leftarrow \mathcal{G}^N \cup \mathbf{v}'$

$\mathcal{U} \leftarrow \mathcal{U} - \{\mathbf{v}'\}$, with

$\mathbf{v}' = \arg\min_{\mathbf{v} \in \mathcal{V}} \{\|\mathbf{DP^r}(\mathbf{g}, \mathbf{v}) \circ \mathbf{w}\|_1\}, \forall \mathbf{g} \in \mathcal{G}^N$, being $\circ$ the Hadamard product operator and $\|\cdot\|_1$ the norm-1 operator.

else

No more candidate IMPCs to be added in the current SMPC:

Candidate IMPCs not evaluated yet $\leftarrow$ NO

end if

end while

end while

$^{(*)}$ Here "$\leqq$" is defined as a multi-dimensional inequality operator, i.e., given $\mathbf{z}^1, \mathbf{z}^2 \in \mathbb{R}^M$ such that $\mathbf{z}^1 = (z_1^1, z_2^1, \ldots, z_M^1)^{\mathrm{T}}$ and $\mathbf{z}^2 = (z_1^2, z_2^2, \ldots, z_M^2)^{\mathrm{T}}$, then $\mathbf{z}^1 \leqq \mathbf{z}^2 \Leftrightarrow z_i^1 \leq z_i^2, \forall i = 1, 2, \ldots, M$.

B. Detection of Long-term Time-Variant MPCs

In Section II, we have showed that the evolution of the delay of the MPCs can be modeled as the square root of a hyperbolic curve plus a constant (see (2)). In this section we will detect the LMPCs by trying to find groups of SMPC whose evolution in delay can be fitted by such an expression, potentially non-continuous due to blockage effects. The parameters of the fit for

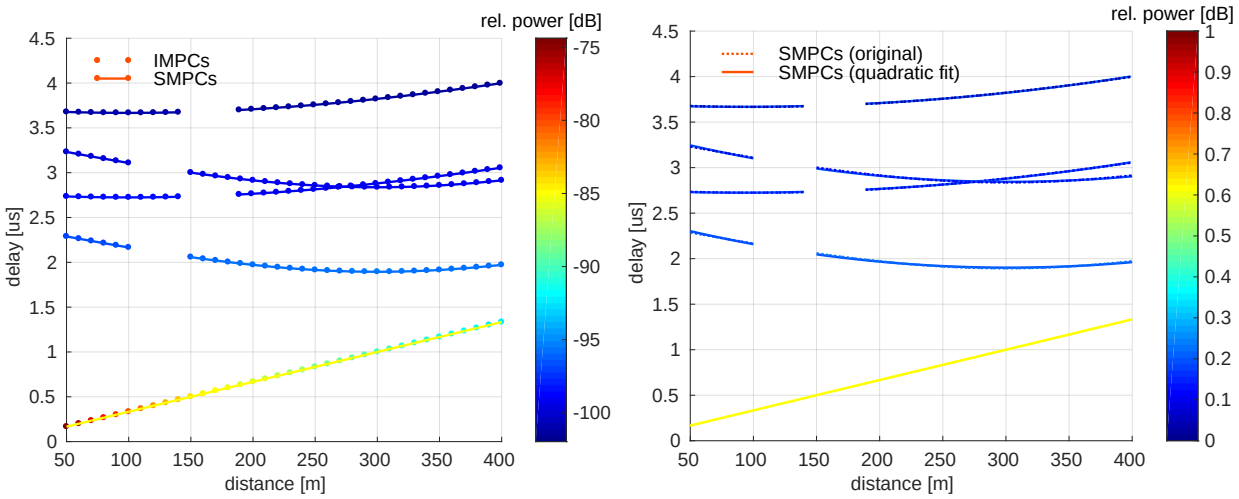

(a) Detected SMPCs.

(b) Quadratic fittings for the detected SMPCs.

Fig. 2: SMPCs detected by the Algorithm 1 for the IMPCs shown in Fig. 1b.

each LMPC will lead also to the analytical geometrical model for the evolution of each MPC. The delay was considered as the key property of the IMPCs in this step since it was found to be more stable than the others (horizontal distance, relative power and Doppler frequency) in the long term. For example, the variation of the Doppler frequency of a MPC over time exhibits much more variance due to aspects such as slight variations of the UAV orientation due to the wind. Moreover, this does not mean that the other MPC properties such as the relative receive power or the Doppler frequency were not considered: *(1)* on the one side, they were considered in Algorithm 1 for the detection of the SMPCs, since they are stable in the short term; and, *(2)* on the other side, they will be examined in Section IV-C to prove that the results obtained by the GSTM are reasonable.

In order to make the algorithm more mathematically tractable, we will approximate the hyperbolic term in (2) by a quadratic curve. As an example, consider the SMPCs previously obtained (see Fig. 2a). Fig. 2b shows the SMPCs as dotted lines together with their associated quadratic fits[8] (as solid lines). Note that it is almost impossible to distinguish the original SMPCs from their corresponding quadratic fits.

Algorithm 2 tries to group SMPCs (from those identified by the Algorithm 1) such that

[8]In this paper we use a least squares (LS) approach to perform the fits by quadratic curves. However, other fitting options would be also possible.

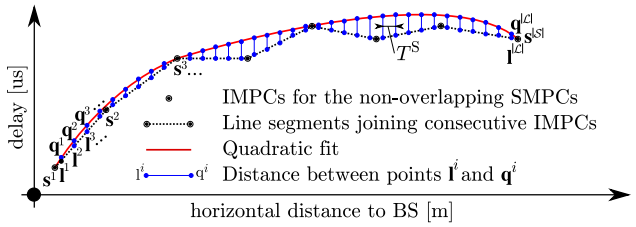

Fig. 3: Example of evaluation of the distance metrics $\mathrm{DH}(\cdot)$ and $\mathrm{DS}(\cdot)$.

the delays of their corresponding IMPCs define geometric patterns similar to quadratic curves over time (or, equivalently, UAV position). The approach starts ordering the SMPCs based on the number of IMPCs they include (from the highest to the lowest[9]). Note that, in principle, SMPCs that belong to a common LMPC should not overlap in horizontal distance. Hence, in each iteration, non-overlapping (in horizontal distance) SMPCs are firstly looked for. For this, we define the overlapping metric between two SMPCs, $\mathcal{A}$ and $\mathcal{B}$, as the number of snapshots for which both $\mathcal{A}$ and $\mathcal{B}$ include an IMPC. Mathematically, the overlapping metric between the SMPCs $\mathcal{A}$ and $\mathcal{B}$, namely $\mathrm{OV}(\mathcal{A},\mathcal{B})$, is defined as

$$\mathrm{OV}(\mathcal{A},\mathcal{B}) = \sum_{i=1}^{|\mathcal{A}|} \mathrm{OVI}(\mathbf{a}^i,\mathcal{B}),\ \ \mathrm{OVI}(\mathbf{x},\mathcal{Y}) = \begin{cases} 1, \text{ if } \exists\, \mathbf{y}\in\mathcal{Y} \mid y_1 = x_1, \\ 0, \text{ otherwise.} \end{cases} \tag{7}$$

Two SMPCs $\mathcal{A}$ and $\mathcal{B}$ are defined as non-overlapping if $\mathrm{OV}(\mathcal{A},\mathcal{B}) \leq d_{\mathrm{OV}}$, for a certain threshold d_{OV}. In most of the cases we may set $d_{\mathrm{OV}} = 0$. However, in some cases in which the MPCs estimates are noisy and the detection of the SMPCs cannot be perfect a moderate value of d_{OV} could eventually improve the obtained results.

A quadratic fit of the trajectory defined by the delays of the IMPCs (ordered by increasing horizontal BS-UAV distance) contained in the non-overlapping SMPCs is obtained. Two distance metrics are defined to evaluate the fit quality. In order to define the distance metrics consider a sample case in which the IMPCs contained in the non-overlapping SMPCs, ordered by increasing horizontal distance, are denoted by $\mathcal{S} = \left\{\mathbf{s}^1, \mathbf{s}^2, \ldots, \mathbf{s}^{|\mathcal{S}|}\right\}$ and plotted in Fig. 3. It is possible to define a line comprised by the segments that join each pair of consecutive IMPCs (represented as the black line in Fig. 3). Let denote by $\mathrm{QF}(\mathcal{S})$ the corresponding quadratic curve, represented

[9]This way, the search of LMPCs starts with the largest SMPCs (i.e., those with the largest number of IMPCs), which should be the most reliable ones.

Algorithm 2 Detection of LMPCs

Let $\mathcal{G}$ be defined as the set comprised by the SMPCs previously created, i.e., $\mathcal{G} := \{\mathcal{G}^1, \mathcal{G}^2, \ldots, \mathcal{G}^{|\mathcal{G}|}\}$
Let $\mathcal{O}$ be defined as the set of all the previously detected SMPCs whose number of IMPCs exceeds N_e, ordered by the number of IMPCs:
$\mathcal{O} := \{\mathcal{G}^i \in \mathcal{G} : |\mathcal{G}^i| > N_e, \ i = 1, 2, \ldots, |\mathcal{G}|\}, \ |\mathcal{O}^1| \geq |\mathcal{O}^2| \geq \cdots \geq |\mathcal{O}^{|\mathcal{O}|}|$.
Initialize $M := 0$ *(index of the current LMPC)*
while $\mathcal{O} \neq \{\emptyset\}$ *(SMPCs not assigned to any LMPC still available)* **do**
  Update the LMPC index and create a new LMPC, namely $\mathcal{T}^M$, containing only the SMPC with the largest amount of IMPCs still not assigned to any LMPC, named $\mathcal{O}^m$ below:
  $M \leftarrow M + 1$
  $\mathcal{O} \leftarrow \mathcal{O} - \{\mathcal{O}^m\}, m = \arg\min_i \mathcal{O}^i \in \mathcal{O}$
  $\mathcal{T}^M := \{\mathcal{O}^m\}$
  Look for SMPCs matching the current LMPC:
  Candidate SMPCs not evaluated yet $\leftarrow$ YES
  while Candidate SMPCs not evaluated yet = YES **do**
    Create an empty set and fill it with the unassigned SMPCs that are non-overlapping with respect to the current LMPC and meet the two metric distance criteria to be included in it:
    $\mathcal{V} := \{\emptyset\}$
    for $i = 1, 2, \ldots, |\mathcal{O}|$ **do**
      if $\text{OV}(\mathcal{O}^i, \mathcal{O}^j) \leq d_{\text{OV}}, \forall \mathcal{O}^j \in \mathcal{T}^M$ **and**
      $\text{DH}(\mathcal{T}^M \cup \mathcal{O}^i) < d^{\text{DH}}$ **and**
      $\text{DS}(\mathcal{T}^M \cup \mathcal{O}^i, d^{\text{DS}}) < p^{\text{DS}}$ **then**
        $\mathcal{V} \leftarrow \mathcal{V} \cup \mathcal{O}^i$
      end if
    end for
    if $\mathcal{V} \neq \{\emptyset\}$ **then**
      If there are candidate SMPCs to be included in the LMPC, select the best one based on the metric distance and update the LMPC:
      $\mathcal{T}^M \leftarrow \mathcal{T}^M \cup \mathcal{O}'$
      $\mathcal{O} \leftarrow \mathcal{O} - \{\mathcal{O}'\}$,
      being $\mathcal{O}' = \arg\min_{\mathcal{O}^i \in \mathcal{V}} \text{DS}(T^M \cup \mathcal{O}^i, d^{\text{DS}})$
    else
      No more candidate SMPCs to be added in the current LMPC:
      Candidate SMPCs not evaluated yet $\leftarrow$ NO
    end if
  end while
end while

by the red curve in Fig. 3. Both lines (the black and the red ones) can be sampled with a certain period T^{DS}, being their respective samples denoted by $\mathcal{L} = \mathbf{l}^1, \mathbf{l}^2, \ldots, \mathbf{l}^{|\mathcal{L}|}$ and $\mathcal{Q} = \mathbf{q}^1, \mathbf{q}^2, \ldots, \mathbf{q}^{|\mathcal{Q}|}$, respectively, where $|\mathcal{Q}| = |\mathcal{L}|$, $\mathbf{l}^i = (l_1^i, l_2^i)^{\text{T}}$ and $\mathbf{q}^j = (q_1^j, q_2^j)^{\text{T}}$, for $i, j = 1, 2, \ldots, \mathcal{L}$. The distance metrics for the quadratic fit quality assessment are defined as follows:

- $\text{DH}(\mathcal{S})$: maximum distance in delay between each pair of samples of $\mathcal{L}$ and $\mathcal{Q}$:

$$\text{DH}(\mathcal{S}) = \max_{i=1,2,\ldots,|\mathcal{L}|} \{|l_2^i - q_2^i|\} \tag{8}$$

- $\text{DS}(\mathcal{S}, d^{\text{DS}})$: proportion of points of the line joining the IMPCs whose distance to their

corresponding counterparts in the quadratic fit exceed certain value d^{DS}:

$$\text{DS}(\mathcal{S}, d^{\text{DS}}) = \frac{|\mathcal{Y}|}{|\mathcal{L}|},\ \mathcal{Y} = \{\text{I}^i \in \mathcal{L} : |l_2^i - q_2^i| > d^{\text{DS}},\ i = 1, 2, \ldots, |\mathcal{L}|\} \tag{9}$$

In each iteration of the Algorithm 2, a set of SMPCs will be accepted as a LMPC if both distance metrics, $\text{DH}(\mathcal{S})$ and $\text{DS}(\mathcal{S}, d^{\text{DS}})$, are below certain predefined thresholds, namely d^{DH} and p^{DS}, respectively. Among the valid fits, the one exhibiting the lowest $\text{DS}(\cdot, d^{\text{DS}})$ value will be selected[10]. As long as we reduce the values of both of d^{DH} or p^{DS}, the quadratic fit needs to be more close to the line of segments that join each par of consecutive IMPCs. Decreasing d^{DH} will reject fits in which any IMPC is far from the fitted curve, however it can make the algorithm unable to find quadratic fits when there is noise in the MPC estimates. p^{DS} tries to ensure that the segments that join the IMPCs included in the fit have a similar trend to that of the fitted curve. Lower values of p^{DS} and d^{DS} ensure that most of the points of the segments joining the corresponding IMPCs are close to their counterparts in the fitted line. However, too low settings can make the algorithm unable to find proper fits and hence not being able to track the long-term stability of the MPCs evolution. Finally, note that decreasing in excess the value of T^{DS} will not improve the results evaluation of the distance metrics and can result in an unnecessary increase of the computational cost. In general, having a few samples between each pair of consecutive IMPCs will be enough.

Once a SMPC is added to a certain LMPC, the process of search of SMPCs that fit in the updated LMPC is restarted. When no more SMPCs match the current LMPC, a new one is created and initialized as including only the SMPC with the largest amount of IMPCs still not included in any LMPC. Only SMPCs with a number of IMPCs larger than a certain threshold N_e are considered for the search of LMPCs, in order to increase the reliability of the results[11].

Fig. 4 presents the results of applying the Algorithm 2 to the simplified case shown in Fig. 1a, by using as input the SMPCs detected by the Algorithm 1. The LMPCs are represented as solid thick red curves and the corresponding SMPCs for each trajectory are also plot overimposed as

[10]In the actual implementation, if $\text{DS}(\cdot, d^{\text{DS}})$ for two fits is equivalent, the one with the lowest sum of distances between the points of the quadratic fit and their counterparts in the line comprised by the segments that join each pair of consecutive IMPCs will be selected.

[11]In general, it is expected that the LMPCs are comprised by stable SMPCs, and hence not including too few IMPCs each. Increasing the value of N_e enables to consider only stable SMPCs and whose trend is better defined (since they include more IMPCs) and hence to avoid fitting erroneous LMPCs. However, a too high N_e setting can result in the algorithm not being able to fit LMPCs that appear and disappear very frequently (hence leading to short SMPCs).

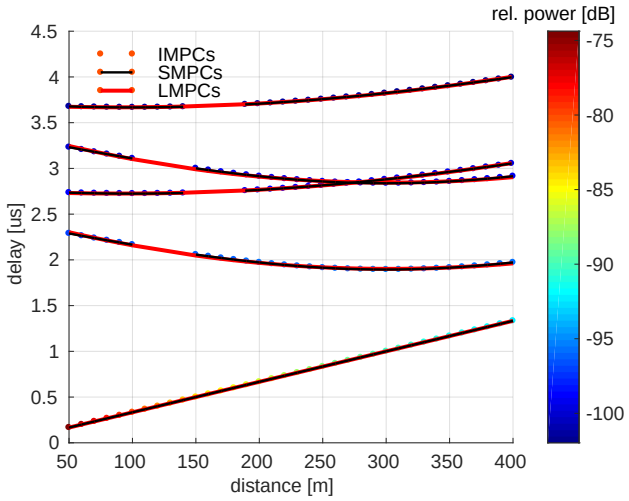

Fig. 4: LMPCs detected by the Algorithm 2 for the SMPCs shown in Fig. 2a.

thin black lines. Each LMPC can be comprised by a single SMPC (e.g., the LoS component case) or several of them (e.g., the scattered components).

One could argue why the GSTM needs to detect the SMPCs (by means of Algorithm 1) in order to obtain the LMPCs (by means of Algorithm 2) instead of directly detecting the LMPCs by looking for geometric patterns defined by the IMPCs in the PDP. Although this approach would be more simple, it would not ensure the short-term spatial consistency of the Doppler frequency and power of the tracked MPCs, leading to potentially incorrect results. Hence, the GSTM, by considering the Algorithm 1 and Algorithm 2, exploits both the short- and long-term spatial consistency of the IMPCs to ensure that the obtained results are realistic.

C. Performance of the GSTM

In order to test the effectiveness of the GSTM, Monte-Carlo simulations were used with random realizations of propagation scenarios. Then, the IMPCs and SMPCs obtained by the GSTM were compared with the theoretical expected results.

The same BS location and flight route as in Fig. 1a were considered. “Last hop” scatterers are generated along the flying route with random distance between consecutive scatterers, random height and random distance to the flight route. Furthermore, each scatterer can be selected to lead to a component with scattering order 1 (i.e., BS $\rightarrow$ last-hop scatterer $\rightarrow$ UAV) or with higher scattering order (i.e., BS $\rightarrow$ scatterer(s) $\rightarrow$ last-hop scatterer $\rightarrow$ UAV) with a given probability. In order to model the cases in which the scattering order is larger than 1, the delay value associated

to the MPCs generated by the last hop scatterer is be increased randomly, and a power loss coefficient (to account for power looses due to successive reflections in multi-scattered signal components). Finally, the MPCs generated by the scatterers can encounter blockage effects. The blockages for each scatterer occur randomly along the flight route and have a random duration. All the parameters of the considered distributions are specified in Table I. Finally, in order to account for the effect of inaccuracies in the IMPCs estimation, we added noise to the generated IMPCs before applying the GSTM. We denote by SNR_{est} the Signal to Noise Ratio (SNR) of the IMPCs estimates. A value of $\text{SNR}_{\text{est}} = 40\,\text{dB}$ would mean that noise is added to the power, delay and Doppler frequency of the IMPCs so that the corresponding SNR for each component is $40\,\text{dB}$.

Value	Distribution	Parameters
Distance between consecutive scatterers	Exponential	$\lambda = 100\,\text{m}$
Dist. between scatterers and flight route	Truncated Gaussian	$\mu = 75\,\text{m}$, $\sigma = 15\,\text{m}$, $[a, b] = [25, 300]\,\text{m}$
Scatterers height	Uniform	$[a, b] = [15, 90]\,\text{m}$
Scattering order higher than 1 (SOHT1)	Bernoulli	$p = 0.3$
Excess of delay (SOHT1 cases)	Truncated Gaussian	$\mu = 0.75\,\mu\text{s}$, $\sigma = 0.5\,\mu\text{s}$, $[a, b] = [0.25, 2]\,\mu\text{s}$
Power loss coefficient (SOHT1 cases)	Uniform	$[a, b] = [0.5, 0.7]\,\mu\text{s}$
Distance between consecutive blockages	Exponential	$\lambda = 200\,\text{m}$
Length of blockage effect	Exponential	$\lambda = 100\,\text{m}$

TABLE I: Parameters of the statistical distributions used for the simulations. *λ is the rate of a exponential distribution, whereas μ and σ denote the mean and the standard deviation of Gaussian distributions. p denotes the success probability of a Bernoulli distribution and a and b are the lower and upper limits, respectively, for uniform or truncated Gaussian distributions.*

For each theoretical SMPC (or LMPC), we firstly identify the SMPC (LMPC) obtained by the GSTM that includes the largest amount of IMPCs contained in the theoretical SMPC (LMPC). Then, we consider all the IMPCs included in both the theoretical SMPC (LMPC) and the one detected by the GSTM as correctly detected. If there are IMPCs in the theoretical SMPC (LMPC) not included in the SMPC (LMPC) detected by the GSTM or the latter includes extra IMPCs, all of them are considered as incorrectly detected. The obtained results are included in Table II. R_{SMPC} denotes the percentage of received power that is included in any SMPC and it is calculated

as $R_{\text{SMPC}} = 100 \cdot P_{\text{SMPC}}/P_{\text{IMPC}} \approx 98.40\%$, where $P_{\text{SMPC}} = \sum_{n=1}^{N} \sum_{m=1}^{|\mathcal{G}^n|} g_2^{n,m}$, $P_{\text{IMPC}} = \sum_{i=1}^{I} \sum_{l=1}^{L} \left|\alpha_{i,l}\right|^2$, N is the total number of detected SMPCs and $g_2^{n,m}$ is the power of the m-th IMPC contained in the n-th SMPC, as defined in Algorithm 1. R_{LMPC} is the percentage of received power that is included in any LMPC as is calculated in an analogous way. C_{SMPC} and C_{LMPC} are the percentages of IMPCs correctly associated to a SMPC or LMPC, respectively. Together with the average values, the corresponding 95% BCa bootstrap confidence intervals for the mean [31] are also provided in the Table II.

SNR_{est} [dB]	R_{SMPC} [%]	R_{LMPC} [%]	C_{SMPC} [%]	C_{LMPC} [%]
∞	99.14 [98.18, 99.58]	98.54 [96.43, 99.48]	96.49 [93.08, 98.60]	93.62 [90.52, 96.98]
40	99.14 [98.36, 99.62]	98.54 [96.39, 99.40]	96.76 [94.16, 99.09]	93.91 [90.82, 96.99]
30	99.13 [98.04, 99.56]	98.55 [96.02, 99.53]	94.88 [90.38, 98.12]	92.92 [89.90, 96.53]
25	98.86 [97.45, 99.45]	97.87 [95.50, 99.08]	90.24 [84.61, 95.83]	89.56 [85.24, 93.85]
20	98.51 [97.91, 99.05]	97.08 [95.70, 98.24]	80.96 [74.91, 89.14]	82.26 [74.92, 89.30]
15	97.47 [96.91, 97.97]	94.69 [91.16, 96.46]	69.83 [61.51, 80.29]	63.17 [55.11, 75.36]

TABLE II: GSTM performance results for different values of IMPCs estimates SNR. Average values together and corresponding 95% BCa bootstrap confidence intervals [31] are provided.

IV. Experimental Results

In this section, the GSTM is applied to actual data obtained from a A2G low-height UAV measurement campaign in a realistic suburban environment and the results are presented. Section IV-A briefly describes the measurement environment as well as the procedure followed for acquiring the signals, whereas Section IV-B shows the obtained results. Finally, Section IV-C analyzes in detail some sample cases to prove that the obtained results are coherent with the propagation geometry.

A. Measurements Environment and Procedure

The data acquired in the measurement campaign detailed in our previous work [8] was used to test the performance of the GSTM. The reader is referred to that work for details regarding the measurement environment as well as the setup used to perform the measurements. However, for the sake of completeness, we will detail the most important aspects below. Section IV-A1

Fig. 5: Considered measurement scenario including the BS and UAV flight route. Some of the buildings are labeled in the map for reference as well as some of the scatterers considered.

defines the considered measurement scenario, whereas Section IV-A2 describes the employed measurement setup. Finally, Section IV-A3 describes the transmit signals as well as the processing performed at the receiver.

1) Measurement Environment: A measurement campaign consisting in horizontal flights at different heights in several suburban scenarios at the Jiading Campus of the Tongji University (Shanghai, China) was performed. In this work, a single flight is considered. The lowest flight height ($15\,$m) and the richest scenario in architectural and natural structures were chosen, so that the influence of the ground elements is more noticeable. The scenario is imaged in Fig. 5. The figure also shows the position of the transmitter[12] (BS), as well as the starting and end points of the flight route[13] (the UAV acts as the receiver). As imaged in Fig. 5, a straight flight in which the UAV flies between several buildings is considered, resulting in an Obstructed LoS (OLoS) environment. The total flight distance is about $450\,$m. Some sample reflection points are also marked in the figure labeled with red characters, being their details provided in Section IV-C.

2) Measurement Equipment: Fig. 6a illustrates a diagram of the equipment transmitting and acquiring the signals. It consists of two parts, namely the air part (which acts as a transmitter) and the ground part (receiver). The air part was loaded on a UAV as illustrated in Fig. 6d, whereas the ground part is mounted at a height-variable tower fixed at a height of $15\,$m (see

[12]Coordinates of the transmitter expressed as (latitude, longitude) are: $(31.2873872^\circ, 121.2040907^\circ)$.

[13]Coordinates of the starting point and end point expressed as (latitude, longitude) are: $(31.287433^\circ, 121.204179^\circ)$ and $(31.288310^\circ, 121.208793^\circ)$.

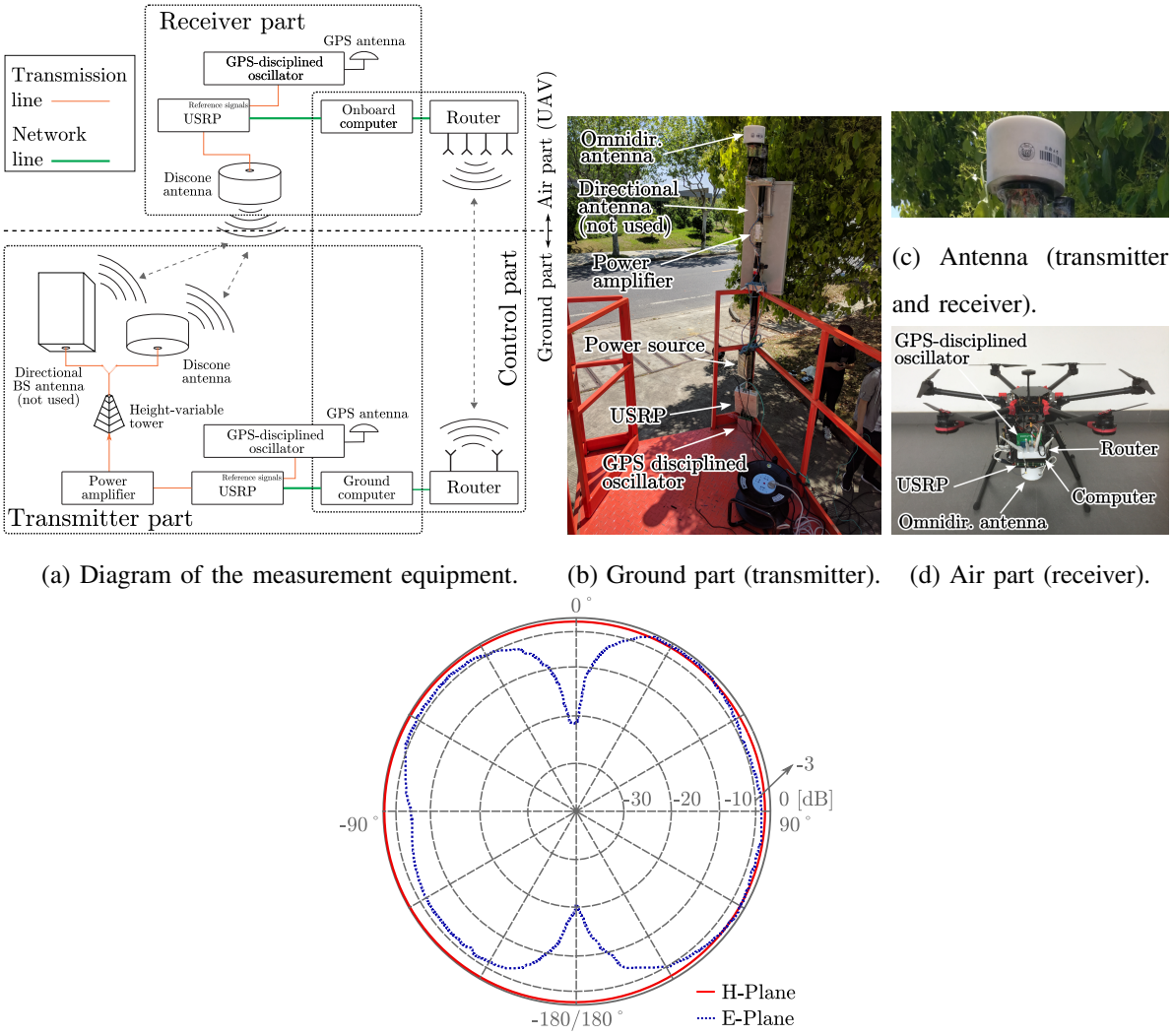

(a) Diagram of the measurement equipment.

(b) Ground part (transmitter).

(c) Antenna (transmitter and receiver).

(d) Air part (receiver).

(e) Radiation pattern of the antenna (transmitter and receiver).

Fig. 6: Measurement equipment.

Fig. 6b). Both air and ground parts include a set of common equipments, which are[14]:

- **Universal Software Radio Peripheral (USRP) N-210**: generates (at the transmitter side) or acquires (receiver side) the signals.
- **GPS-disciplined oscillator**: generates the common reference signals for transmitter/receiver synchronization based on the received Global Positioning System (GPS) information. On the one hand, a 10 MHz signal at both ends enable the synchronization of the transmitter/receiver internal oscillators, which is essential for the accuracy of the obtained results. On the

[14]Note that the cases of several elements were removed in the air part to reduce the size and weight of the onboard equipment.

other hand, the 1 Pulse Per Second (PPS) signal enables synchronization of the sample times for the transmitter and the receiver. This way, the transmitter and receiver share a common absolute time-basis, allowing to estimate the absolute propagation delay. Note that the measurements were geo-localized by using the GPS information as well.

- **Antenna**: two identical quasi-omnidirectional packaged discone antennas (as the one imaged in Fig. 6c) were used at transmitter and receiver sides to minimize the effects of the radiation pattern on the estimated channel characteristics (see the radiation pattern in Fig. 6e). As detailed in [8] and in Figs. 6a and 6b, there is an additional antenna available at the transmitter, which was not used for this study.
- **Computer**: used to control the USRP and store the generated (transmitter) or acquired (receiver) signals. In the case of the UAV, a small-factor computer to reduce the total weight and size of the whole set. Both computers are provided with a self-developed C++ program that uses the USRP hardware driver (UHD) library from Ettus to configure the radio frequency (RF) parameters of the USRPs and send the signal to be transmitted to the USRP (transmitter side) or acquire the received samples from the USRP (receiver side). This program also performs synchronization tasks by means of the signals received from the GPS-disciplined oscillator. Furthermore, in the case of some eventual sample dropping by the limitations of the USRP or the storage media, the receiver is prepared to self-recover itself in less than one second and keep track of the lost samples so that they can be avoided during the processing of the acquired signal.
- **Commercial Wi-Fi router**: allows to establish a local area network between both computers (at the transmitter and receiver) when the UAV is close to the BS to start/stop the signal acquisition at the UAV by the operator at ground. It is worth noting that the routers worked at the frequency band of 2.4 GHz causing no interference to the measurements.

Additionally, the ground node (transmitter) includes a power amplifier, required for increasing the SNR of the results, as well as extending the distance range of the measurements.

3) Signal Generation and Processing: Both for the generation as well as processing of the signals, the so-called "GTEC 5G Simulator" was used [32], [33]. The "GTEC 5G Simulator" is a versatile piece of software that enables to fully configure the transmit signal and includes all the necessary developments for processing the acquired samples, such as channel estimation,

Parameter	Value	Parameter	Value
Transmit power	40 dBm	Sampling frequency	15.36 MSamples/s
Antenna gain	0 dBi (omnidir., UAV and BS)	FFT size	1024 points
BS antenna height	15 m	Used subcarriers	600 (excluding DC)
UAV flight height	15 m	Subcarrier spacing	15 kHz
UAV flight speed	5 m/s	Cyclic prefix length	72 samples
Carrier frequency	2.5 GHz	Estimated paths	15
Bandwidth	15.36 MHz (9 MHz plus guards)	Snapshot rate	1 snapshot/s

TABLE III: Configuration parameters used for the measurements.

interpolation and equalization algorithms, as well as time and frequency synchronization[15]. A High-Resolution Parameter Estimation (HRPE) algorithm, namely SAGE algorithm, similar to that proposed in [34], is used at the "GTEC 5G Simulator" receiver, which allows us to estimate the different parameters of the impinging waves for the acquired signals. More specifically, we consider the delay, the complex-valued amplitude and the Doppler frequency for each path, in accordance with the model presented in (1). For this study, an orthogonal frequency-division multiplexing (OFDM) signal featuring a sampling rate of 15.36 MHz was considered, being the central carrier frequency of 2.5 GHz, values which are similar to those corresponding to commercial LTE deployments in the area of the measurements[16]. The signal, transmitted in a continuous fashion, has a very similar structure to that of the 10 MHz downlink profile of LTE [35]. For our study, we estimated $L = 15$ paths, which were experimentally proved to contain most of the energy of the channel for the considered scenario. The main configuration parameters employed for the measurement campaign are indicated in Table III.

B. Obtained Results

In this section we consider the IMPCs estimated from the acquired signal by applying the SAGE algorithm as an input to the GSTM. In order to firstly present a graphical representation of the estimated IMPCs, we calculated the "instantaneous" PDP for each snapshot by applying (5),

[15]The source code of both the GTEC Testbed and the GTEC 5G Simulator is publicly available under the GPLv3 license at https://bitbucket.org/tomas_bolano/gtec_testbed_public.git.

[16]Note that the 2.5 GHz band is also planned to be used in sub-6 GHz 5G network deployments in China and other countries.

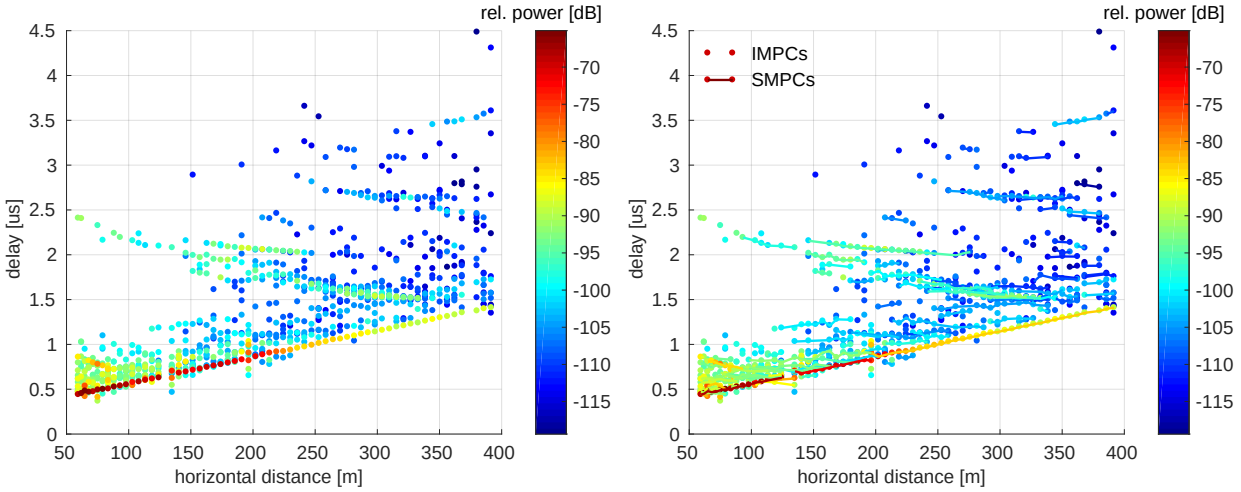

(a) Original PDP.

(b) SMPCs detected by the Algorithm 1.

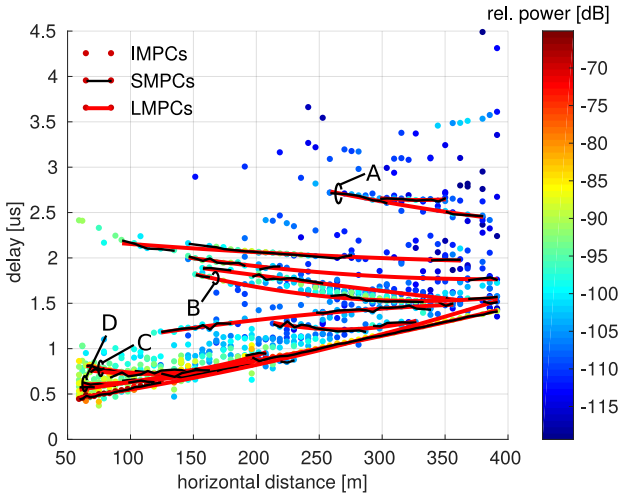

(c) LMPCs detected by the Algorithm 2.

Fig. 7: Results obtained when the Algorithms 1 and 2 are applied to actual received signals.

as detailed in Section II. The results are shown in Fig. 7a, where each dot represents an IMPC. The color of each dot denotes the relative received power, whereas the X axis represents the horizontal distance between the transmitter and the receiver and the Y axis the delay. Similarly to the simplified case presented in Fig. 1b, it can be seen that the distribution of the IMPCs for different snapshots is clearly not independent. On the one hand, a strong LoS contribution can be identified as a set of powerful IMPCs that form a straight line with increasing delay with respect to the horizontal distance between the UAV and the BS, which is coherent with the fact that the UAV speed was constant. However, on the other hand we can see other IMPCs

describing some curves, in a similar fashion as the one presented in Fig. 1b. Finally, there are other IMPCs whose distribution looks more random.

Fig. 7b shows the results of applying the SMPCs detection algorithm (Algorithm 1) to the detected IMPCs. Each two consecutive IMPCs from a common SMPC are joined by a segment. This way, each SMPC is represented by a line comprised by the set of all segments joining pairs of consecutive IMPCs, being the color of the line defined by the average power of all the IMPCs in the SMPC. It can be seen that, similarly to the example shown in Fig. 2a, several of the shown SMPCs tend to define curves in the delay domain. The percentage of received power included in any SMPC (see Section III-C) is $R_{\text{SMPC}} = 98.40\%$. The average length of the detected SMPCs can be obtained as $L_{\text{SMPC}} = \frac{1}{N}\sum_{n=1}^{N}\left(\max_{m=1,\ldots,|\mathcal{G}^n|}\left(g_1^{n,m}\right) - \min_{m=1,\ldots,|\mathcal{G}^n|}\left(g_1^{n,m}\right)\right) \approx 24.40\,\text{m}$, where $g_1^{n,m}$ denotes the horizontal distance between the UAV and the BS for the m-th of the n-th SMPC, as defined in Algorithm 1.

Fig. 7c shows the main LMPCs detected from the SMPCs by means of the Algorithm 2. A LMPC can be comprised by a single SMPC or several. For the sake of clearness, only the LMPCs comprised by more than a single SMPC are plotted in Fig. 7c by thick red lines. The corresponding SMPCs for each LMPC are also plotted overimposed as thin black lines. By comparing Figs. 7a and 7c, it can be seen that the detected LMPCs describe well the observed general trend of the observed IMPCs in the delay domain. It can be seen that some of the LMPCs correspond to SMPCs located far away to each other, which accounts for the cases in which the LMPC is not always active, but it is born and dies in several occasions. Moreover, it can be seen that there are some areas of the plot (e.g., the area for horizontal distances between $250\,\text{m}$ and $350\,\text{m}$) where many LMPCs are not active (no black lines on top of the red ones), to later reappear, which is a result from the blockage of several reflections by large elements of the measurement environment. The percentage of received power included in any LMPC (see Section III-C) is $R_{\text{LMPC}} = 96.24\%$. This confirms that the MPCs exhibiting a regular trend over time with the flight of the UAV contain most of the energy of the channel. The average length of the detected LMPCs is $64.68\,\text{m}$.

It is worth noting that several parameters and thresholds have been defined in the previous algorithms. The considered values, obtained by manual tuning, are specified in Table IV.

parameter	value	parameter	value
$\mathbf{r} = (r_1, r_2, r_3, r_4)^{\mathrm{T}}$	$(17\,\mathrm{m}, 9\,\mathrm{dB}, 0.04\,\mu\mathrm{s}, 4.5\,\mathrm{Hz})^{\mathrm{T}}$	$\mathbf{w} = (w_1, w_2, w_3, w_4)^{\mathrm{T}}$	$(1, 1, 1, 1)^{\mathrm{T}}$
N_e	3 IMPCs	d_{OV}	0 snapshots
d^{DH}	$0.07\,\mu$s	d^{DS}	$0.04\,\mu$s
p^{DS}	0.15	T^{DS}	0.5 m

TABLE IV: Parameters used in Algorithms 1 and 2.

label	d_{S} [m]	d_{U} [m]	h_{S} [m]	description	label	d_{S} [m]	d_{U} [m]	h_{S} [m]	description
A	470	140	35	Telecom. School	C	100	25	10	Media School (I)
B	340	75	70	Library	D	50	35	10	Media School (II)

TABLE V: Coordinates of the scatterers A, B, C and D in Fig. 5. d_{S} denotes the horizontal distance between the scatterer and the BS, whereas d_{U} is the horizontal distance between the scatterer and the flight route and h_{S} the height from the ground.

C. Discussion about the Results

In this section we will discuss the obtained results in more detail and relate them with the underlying propagation environment. In order to do that, we select four of the detected LMPCs as examples, marked with characters from "A" to "D" in Fig. 7c.

Firstly, based on the analytical geometrical model for each sample LMPC (as a quadratic curve) extracted by the Algorithm 2, we identified a scatterer (modeled as a single point) in the environment that can lead to the corresponding IMPCs forming the LMPC. Even if there is not a closed mathematical expression to obtain the element of the environment leading to a specific LMPC from the quadratic model, in many cases it is relatively easy to guess this information by visual inspection of the environment and the parameters of the quadratic curve (see Section III-B). The scatterers selected for the sample LMPCs were marked and labeled with characters from "A" to "D" as well in Fig. 5, whereas their specific coordinates are provided in Table V in terms of the distance to the flight route, the horizontal distance and the height from

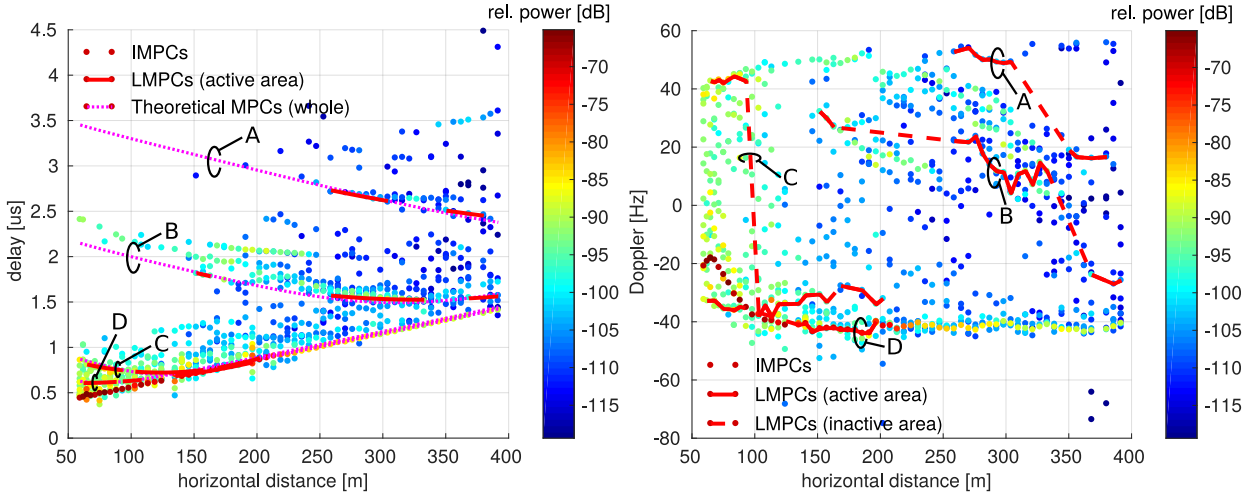

(a) Sample LMPCs and theoretical delay curves. (b) Doppler frequency evolution for the sample LMPCs.

Fig. 8: Results for the sample LMPCs.

the ground[17].

Once the scatterers "A" to "D" are defined in the map, we calculate the theoretical curves in delay domain that the time-evolving MPCs corresponding to those scatterers would create by using (2). Such theoretical curves are plotted in Fig. 8a by means of dotted pink lines. No obstructions were considered for their calculation, i.e., it was assumed the existence of LoS between the BS and the scatterer, as well as between the scatterer and the UAV during the whole flight, as well as it was considered that the reflected power was always large enough to be detected at the UAV. This way, the curves are always visible regardless of the position of the UAV. Fig. 8a also includes (as solid red curves) the representation of the corresponding quadratic curves obtained by the GSTM. In this case, only the areas in which the corresponding LMPCs are visible (i.e., at least one of the SMPCs of the LMPC is active, as represented by the solid black lines in Fig. 7c) are plotted. It can be seen how, indeed, the red curves almost perfectly match the pink ones in the respective ranges where they are defined, which shows that the results obtained can effectively be justified by the geometry of the environment.

[17]The 3-D representation of the scatterers in the map (Fig. 5) does not match their actual coordinates in terms of horizontal distance to the BS and the UAV flight route, especially for high buildings. This is due to two actual points with identical coordinates except for the height are represented at the map as two points whose horizontal distances to the BS (as well as their horizontal distances to the UAV flight trajectory) are different between them. In the calculations, the actual distance values (over a 2-D map) were used.

Taking a closer look to the results, indeed, one may realize that, for example, the reflection caused by the library building (label "B") is mainly visible when the UAV is close enough to the building (between approximately $250\,\text{m}$ to $400\,\text{m}$ in terms of horizontal distance). However, it can be observed that for the horizontal distance values in which the UAV is surpassing to the building, the reflection disappears. This is coherent with the fact that the reflection is caused by some element on top of the building (e.g., the metal parts comprising the air conditioning system), hence, when the UAV flies very close to the building (at a much lower flight height than that of the building), the building itself blocks the line of sight between the scatterer and the UAV. In the case of the reflection caused by the Telecommunications School (label "A"), it is blocked for some horizontal distance values by the library building as well and hence the LMPC is not always visible. In the cases of the reflections caused by the Media School (labels "C" and "D"), once the scatterer points are overpassed by the UAV, the delays almost converge to the delay of the LoS path, and hence their contributions cannot be distinguished anymore.

Although, as justified in Section III-B, the delay is a key parameter for detecting the LMPCs, it is also interesting to see how the Doppler frequency of the LMPCs evolves. We define the "instantaneous" Doppler power spectral density (PSD) for the i-th snapshot in an equivalent approach to that used for the PDP in (5), as it was also defined in our previous works [8], [26]:

$$D_i(\nu) = \sum_{l=1}^{L} |\alpha_{i,l}|^2 \delta(\nu - \nu_{i,l}). \tag{10}$$

Fig. 8b shows the Doppler frequency PSD, where each dot represents an IMPC. The color of each dot denotes the relative received power, whereas the X axis represents the horizontal distance between the transmitter and the receiver and the Y axis the Doppler frequency. The Doppler frequency values for the IMPCs with the highest powers are coherent with the low speed considered for the UAV (it can be seen that the speed at the beginning of the flight is still increasing until reaching the target value, $5\,\text{m/s}$). The red curves in Fig. 8b correspond to those in Fig. 8a, i.e., represent the evolution in Doppler of the four sample LMPCs. The active areas of the LMPC (i.e., at least one of the SMPCs is visible) are represented in solid lines, whereas the inactive in dashed ones. It is easy to see that the results in Doppler frequency are coherent with the scatterers identified in Fig. 5. Indeed, it can be seen that, for example, the Doppler changes from positive sign to negative somewhere in the period when the UAV is passing by the library for the LMPC corresponding to the reflection in such a building (label

"B"). A similar effect of change of the sign of the Doppler frequency can be appreciated for the LMPC labeled as "C". In this case, the Doppler changes abruptly from around $40\,\text{Hz}$ to close to $-40\,\text{Hz}$ when the second scatterer at the Media School is overpassed by the UAV. In the case of the scatterer labeled as "D" the Doppler always keeps a negative sign since for the range of horizontal distances presented in Fig. 8b the scatterer is always behind the UAV for the represented range of horizontal distances. For the case of the scatterer at the Telecommunications School, the contrary holds, i.e., the Doppler is always positive, since the UAV never overpasses the scatterer.

V. Conclusions

In this paper, a simplified model for the channel MPCs inherent to the propagation for A2G low-height UAV communications was studied. The model allows to analytically obtain the evolution of the delay of the different MPCs based on the geometry of the propagation channel and includes the case of MPCs that are born and die in several occasions due to blockage by elements of the propagation environment. Based on this simplified model, a novel method for tracking the channel MPCs of A2G low-height UAV, namely the GSTM, without knowledge of the propagation environment, was presented. The GSTM is able to detect the long-term spatial consistency of the MPCs by effectively supporting the tracking of MPCs that disappear for long periods of time (birth/death processes due to blockage by elements of the propagation environments). Moreover, the GSTM not only tracks the evolution of the MPCs, but also provides an analytical geometrical model for the variation of each MPC, which in particular can be used to detect which elements of the propagation environment lead to the different main MPCs. It was shown by means of measurements obtained in a suburban scenario that the GSTM succeeds in tracking the evolution of the MPCs in a real scenario and that the analytical model for the MPCs obtained by the GSTM fits well to the characteristics of the propagation environment and the theoretical expected results.

Our work also shows that in the propagation for A2G low-height UAV communications most of the energy received has a well-defined structure and is consistent on time. What is more, very simplified analytical approaches can effectively describe the propagation of most of the channel energy and justify non-intuitive effects in the propagation channel characteristics studied in our previous works. Hence, the results obtained by the GSTM will be the basis for the establishment of new non-stationary channel models. Finally, the GSTM can be applied to other scenarios

involving relative movement between the transmitter and receiver and frequent LoS conditions between the transmitter and the main scatterers, as well as between those scatterers and the receiver. Common scenarios fulfilling this criteria can be found in Vehicle-to-Vehicle (V2V) or V2I communications, such as in high-speed train (HST) or cars-to-roadside elements, especially in clutter environments, such as urban or suburban. In these scenarios, the GSTM can have much better performance than the existing methods, which do not rely on geometrical propagation properties.

REFERENCES

[1] M. G.-R. H. Fretes, J. Rodríguez-Piñeiro, J. Rodas, and R. Gregor, "Automatic scene reconstruction algorithm for planialtimetric applications," in *XXIII IEEE Congress of the Chilean Association of Automatic Control (ICA-ACCA 2018)*, Concepción, Chile, October 2018.

[2] F. G. Costa, J. Ueyama, T. Braun, G. Pessin, F. S. Osório, and P. A. Vargas, "The use of unmanned aerial vehicles and wireless sensor network in agricultural applications," in *2012 IEEE International Geoscience and Remote Sensing Symposium*. IEEE, 2012, pp. 5045–5048.

[3] C. Torresan, A. Berton, F. Carotenuto, S. F. Di Gennaro, B. Gioli, A. Matese, F. Miglietta, C. Vagnoli, A. Zaldei, and L. Wallace, "Forestry applications of UAVs in Europe: A review," *International Journal of Remote Sensing*, vol. 38, no. 8-10, pp. 2427–2447, 2017.

[4] S. Hayat, E. Yanmaz, and R. Muzaffar, "Survey on unmanned aerial vehicle networks for civil applications: A communications viewpoint," *IEEE Communications Surveys & Tutorials*, vol. 18, no. 4, pp. 2624–2661, 2016.

[5] A. Osseiran, F. Boccardi, V. Braun, K. Kusume, P. Marsch, M. Maternia, O. Queseth, M. Schellmann, H. Schotten, H. Taoka *et al.*, "Scenarios for 5G mobile and wireless communications: the vision of the METIS project," *IEEE Communications Magazine*, vol. 52, no. 5, pp. 26–35, 2014.

[6] 3rd Generation Partnetship Project (3GPP), "UAS – UAV," online access: https://www.3gpp.org/uas-uav.

[7] A. A. Saleh and R. Valenzuela, "A statistical model for indoor multipath propagation," *IEEE Journal on selected areas in communications*, vol. 5, no. 2, pp. 128–137, 1987.

[8] J. Rodríguez-Piñeiro, T. Domínguez-Bolaño, X. Cai, Z. Huang, and X. Yin, "Air-to-ground channel characterization for low-height UAVs in realistic network deployments," *IEEE Trans. Antennas Propag.*, vol. Early Access, 2020.

[9] R. He, B. Ai, G. L. Stüber, G. Wang, and Z. Zhong, "Geometrical-based modeling for millimeter-wave mimo mobile-to-mobile channels," *IEEE Transactions on Vehicular Technology*, vol. 67, no. 4, pp. 2848–2863, 2018.

[10] R. He, C. Schneider, B. Ai, G. Wang, Z. Zhong, D. A. Dupleich, R. S. Thomae, M. Boban, J. Luo, and Y. Zhang, "Propagation channels of 5g millimeter-wave vehicle-to-vehicle communications: Recent advances and future challenges," *IEEE Vehicular Technology Magazine*, vol. 15, no. 1, pp. 16–26, 2020.

[11] Pei-Jung Chung and J. F. Bohme, "Recursive EM and SAGE-inspired algorithms with application to DOA estimation," *IEEE Transactions on Signal Processing*, vol. 53, no. 8, pp. 2664–2677, Aug 2005.

[12] J. Salmi, A. Richter, and V. Koivunen, "Detection and tracking of MIMO propagation path parameters using state-space approach," *IEEE Transactions on Signal Processing*, vol. 57, no. 4, pp. 1538–1550, April 2009.

[13] T. Jost, W. Wang, U. Fiebig, and F. Perez-Fontan, "Detection and tracking of mobile propagation channel paths," *IEEE Transactions on Antennas and Propagation*, vol. 60, no. 10, pp. 4875–4883, Oct 2012.

[14] X. Yin, G. Steinbock, G. E. Kirkelund, T. Pedersen, P. Blattnig, A. Jaquier, and B. H. Fleury, "Tracking of time-variant radio propagation paths using particle filtering," in *2008 IEEE Intl. Conference on Communications*, May 2008, pp. 920–924.

[15] C. Huang, R. He, Z. Zhong, Y. Geng, Q. Li, and Z. Zhong, "A novel tracking-based multipath component clustering algorithm," *IEEE Antennas and Wireless Propagation Letters*, vol. 16, pp. 2679–2683, 2017.

[16] J. Karedal, F. Tufvesson, N. Czink, A. Paier, C. Dumard, T. Zemen, C. F. Mecklenbrauker, and A. F. Molisch, "A geometry-based stochastic MIMO model for vehicle-to-vehicle communications," *IEEE Transactions on Wireless Communications*, vol. 8, no. 7, pp. 3646–3657, July 2009.

[17] X. Cai, X. Yin, X. Cheng, and A. P. Yuste, "An empirical random-cluster model for subway channels based on passive measurements in UMTS," *IEEE Transactions on Communications*, vol. 64, no. 8, pp. 3563–3575, Aug 2016.

[18] C. Huang, A. F. Molisch, Y. Geng, R. He, B. Ai, and Z. Zhong, "Trajectory-joint clustering algorithm for time-varying channel modeling," *IEEE Transactions on Vehicular Technology*, pp. 1–1, 2019.

[19] X. Cai, B. Peng, X. Yin, and A. P. Yuste, "Hough-transform-based cluster identification and modeling for V2V channels based on measurements," *IEEE Transactions on Vehicular Technology*, vol. 67, no. 5, pp. 3838–3852, May 2018.

[20] P. Hanpinitsak, K. Saito, J. Takada, M. Kim, and L. Materum, "Multipath clustering and cluster tracking for geometry-based stochastic channel modeling," *IEEE Trans. Antennas Propag.*, vol. 65, no. 11, pp. 6015–6028, 2017.

[21] K. Mahler, W. Keusgen, F. Tufvesson, T. Zemen, and G. Caire, "Tracking of wideband multipath components in a vehicular communication scenario," *IEEE Transactions on Vehicular Technology*, vol. 66, no. 1, pp. 15–25, 2017.

[22] C. Huang, A. F. Molisch, Y. Geng, R. He, B. Ai, and Z. Zhong, "Trajectory-joint clustering algorithm for time-varying channel modeling," *IEEE Transactions on Vehicular Technology*, vol. 69, no. 1, pp. 1041–1045, 2020.

[23] C. Lai, R. Sun, C. Gentile, P. B. Papazian, J. Wang, and J. Senic, "Methodology for multipath-component tracking in millimeter-wave channel modeling," *IEEE Trans. Antennas Propag.*, vol. 67, no. 3, pp. 1826–1836, 2019.

[24] X. Cai, J. Rodríguez-Piñeiro, X. Yin, N. Wang, B. Ai, G. F. Pedersen, and A. P. Yuste, "An empirical air-to-ground channel model based on passive measurements in LTE," *IEEE Trans. Veh. Technol.*, vol. 68, no. 2, pp. 1140–1154, 2019.

[25] A. F. Molisch, *Wireless communications*. John Wiley & Sons, 2012, vol. 34.

[26] T. Domínguez-Bolaño, J. Rodríguez-Piñeiro, J. A. García-Naya, X. Yin, and L. Castedo, "Measurement-based characterization of train-to-infrastructure 2.6 GHz propagation channel in a modern subway station," *IEEE Access*, vol. 6, pp. 52 814–52 830, September 2018.

[27] A. Meijerink and A. F. Molisch, "On the physical interpretation of the Saleh–Valenzuela model and the definition of its power delay profiles," *IEEE Trans. Antennas Propag.*, vol. 62, no. 9, pp. 4780–4793, 2014.

[28] H. T. Friis, "A note on a simple transmission formula," *Proceedings of the IRE*, vol. 34, no. 5, pp. 254–256, 1946.

[29] C. M. Tan, M. A. Beach, and A. R. Nix, "Enhanced-sage algorithm for use in distributed-source environments," *Electronics Letters*, vol. 39, no. 8, pp. 697–698, 2003.

[30] C. M. Tan and M. A. Beach, "Estimation of propagation channel parameters using multi-dimensional hybrid-space sage algorithm," *IET Microwaves, Antennas Propagation*, vol. 1, no. 6, pp. 1212–1222, 2007.

[31] B. Efron and D. V. Hinkley, *An Introduction to the Bootstrap (CRC Monographs on Statistics & Applied Probability)*, 1st ed. United States: Chapman & Hall, 1994.

[32] T. Domínguez-Bolaño, J. Rodríguez-Piñeiro, J. A. García-Naya, and L. Castedo, "The GTEC 5G link-level simulator," in *1st International Workshop on Link- and System Level Simulations (IWSLS2 2016)*, Vienna, Austria, July 2016.

[33] "GTEC Testbed Project," https://bitbucket.org/tomas_bolano/gtec_testbed_public.git.

[34] B. H. Fleury, M. Tschudin, R. Heddergott, D. Dahlhaus, and K. I. Pedersen, "Channel parameter estimation in mobile radio environments using the SAGE algorithm," *IEEE J. Sel. Areas Commun.*, vol. 17, no. 3, pp. 434–450, 1999.

[35] ETSI, "TS 136 213 V14.2.0: LTE; E-UTRA; Physical layer procedures," April 2017.